Effect of B-site cationic substitution on the structural, spectroscopic, and conductivity behaviour of $Ho_2(Hf_{1-x}Zr_x)_2O_7$ (x=0 and 1)

Md Kashif Shamim [b], Girish M. Kale [a],[*], Suneela Sardar [a], Digvijay Narayan Singh [c], Seema Sharma [b], Ashok Kumar Yadav [d], Shambhu Nath Jha [d], Dibyendu Bhattacharyya [d], Ram Janay Choudhary [e]

[a] School of Chemical Process and Engineering, University of Leeds, UK
[b] Material Research Laboratory, Department of Physics, A N College, Patna, 800013, India
[c] Department of Materials Engineering, Indian Institute of Science Bengaluru, 560012, India
[d] Atomic & Molecular Physics Division, Bhabha Atomic Research Centre, Mumbai, 400 094, India
[e] UGC-DAE Consortium for Scientific Research Centre, Indore, 452001, India

ARTICLE INFO

ABSTRACT

Ideally, a solid electrolyte which is a central component of SOFC should exhibit high anionic or cationic ionic conductivity at the proposed operating temperatures. In most cases, the performance is compromised when operating above 1000 °C due to poor mechanical, thermal and chemical stability of selected functional and non-functional materials. In this context, pyrochlores are one of the potential candidates due to their high conductivity, flexibility to accommodate large cations, and high mechanical, thermal and chemical stability. In this study, we report the synthesis of nano-powders of $Ho_2Hf_2O_7$ (HH) and $Ho_2Zr_2O_7$ (HZ) pyrochlore ceramics by eco-friendly alginate mediated ion-exchange process also known as Leeds Alginate Process (LAP) and provide further insight into the structure - conductivity relationship of HH and HZ compounds by EXAFS studies. Both the compositions were sintered at temperatures, ranging from 1100 °C-1500 °C at 2 h dwell time to achieve the desired high-density ceramic with stable pyrochlore structure. X-ray diffraction and Extended X-ray absorption fine structural (EXAFS) analysis showed superlattice reflections and complex coordination geometry of these oxides. The coordination number and disorder factor in the case of HZ were found to be more stable than the HH sample, as evident from the EXAFS. Impedance spectroscopy and dc-conductivity analysis showed a better charge transport behavior in HZ ceramics than in HH making HZ as a preferred solid electrolyte for SOFC. The conductivity of $Ho_2Zr_2O_7$ is comparable with the best-known fluorite oxide-ion conductor such as Sc_2O_3-stabilized ZrO_2 at 500 °C.

1. Introduction

Solid oxide fuel cells (SOFC) are electrochemical energy devices that provide clean energy (heat and electricity) and exhibit high fuel conversion efficiency [1,2]. Electrolytes are one of the essential components of SOFCs, which acts like an impervious membrane capable of allowing ionic diffusion across the electrolyte/anode and electrolyte/cathode interfaces [3]. Electrolytes are designed to possess high ionic conductivity ($0.01–0.1Sm^{-1}$), low porosity, inertness to redox reaction, lower thickness to reduce Ohmic losses, high mechanical, chemical and thermal stability, compatibility with anode and cathode materials, and materials that can conduct predominantly O^{2-} ions [4,5]. Due to the

desired ionic conductivity, yttria-stabilized zirconia (YSZ) is one of the frequently used materials as solid electrolytes in a commercial SOFC. However, it has been observed that YSZ showed high ohmic loss, high polarization resistance, and low ionic conductivity, when operated at the intermediate temperature ranging between 400 and 800 °C [6]. Therefore, the quest for alternate electrolyte materials with ionic conductivity values comparable with that of YSZ or higher and greater stability in the intermediate operating temperature range is desirable. Materials for ceramic electrolytes and electrodes with crystal structures such as Aurivillius structure [7], Brownmillerite [8], Perovskites [9,10], and Pyrochlore [11] have been extensively investigated. The pyrochlore ($A_2B_2O_7$) materials showed comparable ionic conductivity values to YSZ

when operated in higher temperature regions [12]. In the pyrochlore structure, mono-, di-, and trivalent rare earth can occupy A-sites, and 3*d*, 4*d*, and 5*d* elements can be accommodated at B-sites. Thus, extensive chemical flexibility and ability to host cations with mixed oxidation states can be utilized to tailor these ceramics to deliver the desired mechanical, chemical, thermal and electrical characteristics [12]. Furthermore, the diverse oxidation states add flexibility to adjust the degree of disordering in the pyrochlores and providing better thermal stability to the pyrochlore compounds [13].

It is quite evident that no electrolyte material can totally meet all of the necessary parameters, including high conductivity, greater electrode compatibility, and overall stability. Therefore tailoring A-site cationic charge-states leads to the formation of anion-vacancies in the structure, which are highly responsible for the increase in conductivity, as reported previously for Sm$_{2-x}$Ca$_x$Zr$_2$O$_7$ [14], Nd$_{2-x}$Sr$_x$Zr$_2$O$_7$ [15], Y$_{2-x}$Ca$_x$Ti$_2$O$_7$ [16], Gd$_{2-x}$Sr$_x$Zr$_2$O$_7$ [17], La$_{2-x}$Ca$_x$ Zr$_2$O$_7$ [18] compounds. However pure pyrochlores such as Eu$_{2.096}$Hf$_{1.904}$O$_{6.952}$ and Gd$_2$Hf$_2$O$_7$ compounds have been prepared by conventional solid-state route and sintered at 1600 °C and 1670 °C respectively, exhibited bulk conductivity as high as 5×10^{-3} S cm^{-1} and 3×10^{-3} S cm^{-1} respectively [19].

On the other hand, B-site disordered systems endow a new insight to study the order/disorder transformation and is quite intriguing to explore the disordering impact on the charge transport properties of the pyrochlores [19]. It will be therefore interesting to investigate the efficacy of the crystal structure and the correlated physical characteristics of the pyrochlore compound in which the B-site cations introduce disorder. This study probes the synergistic roles of B-site disordering on the pyrochlore phase and its impact on the ionic behavior of the potential electrolyte materials, Ho$_2$Hf$_2$O$_7$ (HH) and Ho$_2$Zr$_2$O$_7$ (HZ) nanopowders synthesized at less than 600 °C employing an environmentally friendly Leeds Alginate powders (LAP) method. Leeds Alginate powders (LAP) has been successfully shown to yield single-phase high purity nanopowders of catalytically active NiO/NiO$_2$, Gadolinium doped Ceria (GDC) Oxides, and many more complex oxides and their solutions at temperatures lower than 600 °C for SOFC electrolyte/electrode application. Our team has successfully developed the eco-friendly LAP simple sol-gel method to produce nanopowders at temperature far below 600 °C [20–23]. In this study, we will describe the sintering behavior and ionic conductivity effect in Ho-based pyrochlores for SOFCs. Exploring the cationic lattice and its impact on electrical conductivity from the standpoint of SOFC electrolyte application will be intriguing and opening new avenue of research using LAP.

2. Materials and method

Holmium(III) nitrate pentahydrate, Ho(NO$_3$)$_3$*5H$_2$O, Hafnium(IV) tetrachloride, HfCl$_4$, were purchased from Alfa Aesar (Heysham, UK) and Zirconium(IV) oxychloride octahydrate, ZrOCl$_2$*8H$_2$O, was procured from Sigma Aldrich Ltd (Gillingham, UK) all with greater than 99.5% purity. High purity Sodium alginate powder with a general formula (C$_6$H$_7$NaO$_6$)$_n$ was purchased from Sigma Aldrich Ltd (Birmingham, UK). Sodium alginate has a varying combination of 1,4-linked β-mannuronic acid (M) and α-L Guluronic acid (G) residue polymer linked covalently in different sequence such as -MM-, -GG- or -GM- block copolymers, which is readily extracted from brown seaweed and purified [20–23]. Gelation in the alginate is due to carboxylate anion interaction with metal cations such as Ho^{3+} and Hf^{4+} or Ho^{3+} and Zr^{4+} present in 1:1 M ratio in the aqueous medium. 4 wt% of alginate powder is dissolved in deionized water under high frequency stirring at room temperature (say solution-1). In another 200 ml beaker, each of the stoichiometrically weighed Ho/Hf (say solution-2) and Ho/Zr (say solution-3) precursor powders were dissolved in deionized water under constant high frequency stirring. The overall cationic concentration was limited to 30 gm/L, until a clear solution is formed. Alginate beads containing the metal ions were prepared by dripping separately 200 ml

of sodium alginate solution-1 into solution 2 and 3 respectively, using a 16 gauge equivalent to 1.194 mm inner diameter stainless steel needle attached to 20 ml hypodermic syringe with 20 cm^3 volume capacity. The beads were maintained in gelling medium for 24 h under mild stirring for complete ion-exchange to take place. Beads were spherical with average diameter ranging from 4 to 5 mm. Subsequent step involves washing of the beads with deionized water several times and drying it in convection oven for 2 h at 90 °C details of which are described elsewhere [20–23].

As prepared, dried beads were calcined at 700 °C to obtain nanopowders, pelletized and sintered at 1100–1500 °C, each with 2 h dwell time. Structural transition as a function of sintering temperature was studied by employing X-ray diffraction (Bruker D8) equipped with Ni-filtered Cu-kα radiation having λ = 1.5406 Å. The crystallographic parameters were refined using Fullprof software, lattice parameter and other constraints were varied and Pseudo-Voigt function was applied during the Rietveld refinement process [24,25]. For electrical measurements, the silver paste was applied on both sides of the pellet and heated at 800 °C for 1 h for improving surface adhesion. The conductivity of samples was measured using computer controlled Solartron SI1260 from 100 Hz to 1 MHz using Z-view software and the data were analysed by fitting to the selected best-fit equivalent circuit using Z-plot software. The pellets were mounted in a spring-loaded quartz rig with electrical contact made by Pt gauze spot welded to Pt wires. This assembly was placed in a stainless-steel tube acting as a Faraday cage located in a horizontal tube Lenton furnace with the sample pellet positioned in the constant temperature zone at all time. A K-type thermocouple was placed close to the sample for monitoring temperature adjacent to the rig, and the measurement was performed at each temperature.

2.1. Spectroscopic characterizations

X-ray Absorption spectroscopy (XAS) comprising of both X-ray Near-Edge Structure (XANES) and Extended X-ray Absorption Fine Structure (EXAFS) techniques were carried out on Ho$_2$Hf$_2$O$_7$ (HH) and Ho$_2$Zr$_2$O$_7$ (HZ) samples to probe the local structure of the samples. The XAS measurements have been carried out at the Energy Scanning EXAFS beamline (BL-9) at Indus Synchrotron Source (2.5 GeV, 100 mA) at Raja Ramanna Centre for Advanced Technology (RRCAT), India [26,27]. This beamline operates in the energy range of 4 keV–25 keV. The beamline optics consists of Rh/Pt coated collimating meridional cylindrical mirror and collimated beam reflected by the mirror is monochromatized by a Si (111) (2d = 6.2079 Å) based Double Crystal Monochromator (DCM). The second crystal of DCM is a sagittal cylinder used for horizontal focusing, while a Rh/Pt coated bendable post mirror facing down is used for vertical focusing of the beam at the sample position. Rejection of the higher harmonics content (produced during EXAFS measurement) in the X-ray beam is performed by detuning the second crystal of DCM. In the present case, XAS measurements have been performed in transmission mode for all the samples. For transmission measurements, three ionization chambers (300 mm length each) have been used for data collection, one ionization chamber for measuring incident flux (I$_o$), the second one for measuring transmitted flux (I$_t$), and the third ionization chamber for measuring XAS spectrum of a reference gold foil for energy calibration. To improve the signal-to-noise ratio, appropriate gas pressure and gas mixtures have been chosen to achieve 10–20 % absorption in the first and 70–90 % in the second. The absorption coefficient μ was obtained using the relation:

$$I_t = I_o \, e^{-\mu x} \tag{1}$$

To take into account of the oscillations in absorption spectra μ(E) has been converted to absorption function χ$^{(E)}$ defined by the following expression,

$$\chi^{(E)} = (\mu(E) - \mu_o(E))/\Delta\mu_o(E_o) \tag{2}$$

where E_o is the absorption edge energy, $\mu_o(E_o)$ is the bare atom background, and $\Delta\mu_o(E_o)$ is the step value in $\mu(E)$ value at the absorption edge. The energy-dependent absorption coefficient $\chi^{(E)}$ has been converted to the wave number (k) dependent absorption coefficient $\chi(k)$ using the relation,

$$k = \sqrt{2}\, m(E-E_o)/\hbar^2 \tag{3}$$

where m is the electron mass. $\chi^{(k)}$ is weighted by k^2 to amplify the oscillation at high k, and the $\chi(k)k^2$ functions are Fourier transformed to generate the $\chi(R)$ versus R plots in terms of the real distances from the center of the absorbing atom. The EXAFS data analysis programs available within the Demeter software package have been used for EXAFS data analysis. This includes background reduction, Fourier transforms to derive the $\chi(R)$ versus R plots from the absorption spectra (using ATHENA software), generation of the theoretical EXAFS spectra starting from an assumed crystallographic structure, and finally, fitting of experimental data with the theoretical spectra using ARTEMIS software.

3. Results and discussion

3.1. Structural analysis

Figs. 1 and 2 show the evolution of the cubic-pyrochlore (Fd-3m) phase from a defect-fluorite (Fm-3m) phase in HH and HZ samples with increasing sintering temperatures. Some super lattice reflections (SSR) are observed in the lower sintering temperatures (1100–1400 °C), which vanished at 1500 °C for HH and 1300 °C for HZ ceramics. Fig. 3 shows the Rietveld refined X-ray patterns of HZ and HH samples sintered at 1300 °C and 1500 °C, respectively. HZ and HH samples are crystallized in cubic symmetry having the Fd-3m space group, confirming the respective pyrochlore structure. The arrows indicate super-lattice reflections (SSR) of {311}, {331}, and {551} planes of the cubic-pyrochlore system. Such variation in SSR intensity can be attributed to the cationic anti-site disordering/ordering, distribution of oxygen vacancies, processing parameters, and the difference of average scattering factors of elements involved [28]. It isn't easy to refine occupancies of anions or cations using simple XRD data; therefore, we cannot probe the exact amount of ordering/disordering in these oxides. However, the diminished intensities of these SSR peaks indicate that the systems have complex coordination states of cations consistent with previous report [29]. Also, the ionic radii ratios (r_A/r_B) of the HH sample (Ho^{3+}/Hf^{4+}) and HZ sample (Ho^{3+}/Zr^{4+}) are 1.43 and 1.41, respectively, which are very close to pyrochlore compounds exhibiting order-disorder transformations [30], consistent with phase diagrams and previous reports
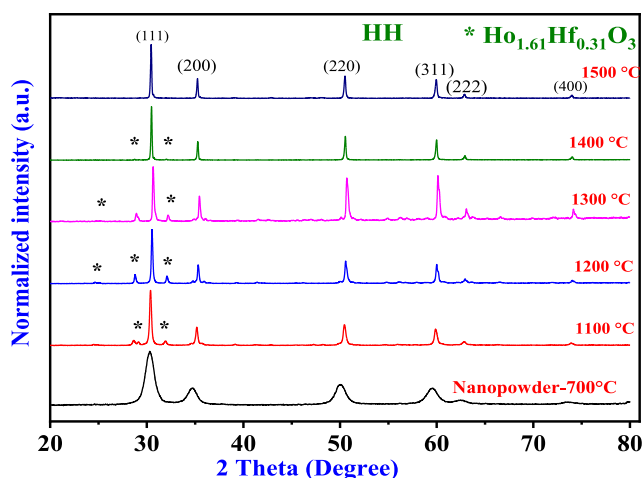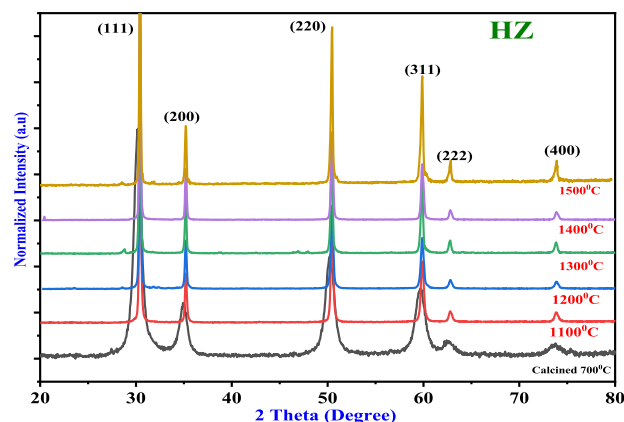

Fig. 2. XRD patterns of HZ sintered at different temperatures.
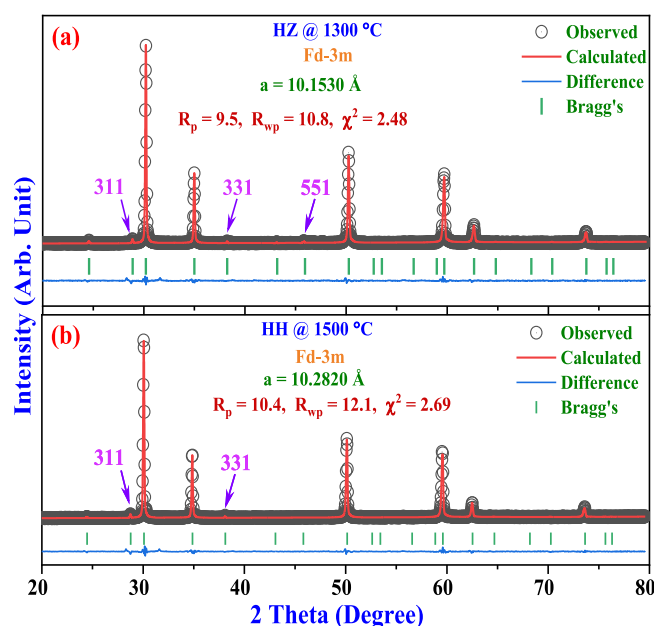

Fig. 3. Rietveld refined XRD patterns of HZ (a) and HH (b) sintered at 1300 °C and 1500 °C, respectively. Black colored circles represent observed XRD data points, the red color solid curves show the calculated pattern, blue color curves show the difference between observed and calculated data points, and green color strips show the respective Bragg's positions. Purple color arrows show the super-lattice reflections (SSR). (For interpretation of the references to color in this figure legend, the reader is referred to the Web version of this article.)

[30–33]. Thus, we can conclude that the pyrochlore phase had formed in the HH sample when it was sintered at 1500 °C, whereas in the HZ samples, it was achieved at 1300 °C. Using Debye-Scherrer's formula the average crystallite size of the sintered HH and HZ samples was calculated at each of the sintering temperature. As anticipated, the crystallite size increased with increasing temperature from 35 to 109 nm and 51–97 nm, while the micro-strain% decreased from 0.31-0.10 and 0.28-0.08 for HH and HZ sample respectively and is listed in Table-1.

3.2. XANES and EXAFS analysis

The super-lattice reflections observed in Rietveld refined XRD patterns of HH and HZ samples sintered at 1500 °C allude to the transition of defect-fluorite to the cubic-pyrochlore structure. Such evolution influences the electronic charge states of the cations. Therefore,

Fig. 1. XRD patterns of HH sintered at different temperatures.

Table 1
Average crystallite size and micro-strain recorded for HH and HZ samples.

Sintering Temperature °C	Crystallite Size nm		Micro-Strain%	
	HH	HZ	HH	HZ
700°C Calcined Nanopowders	6.0	8	1.18	2.04
1100°C Sintered Pellets	35	51	0.31	0.28
1200°C Sintered Pellets	65	59	0.25	0.23
1300°C Sintered Pellets	67	64	0.18	0.21
1400°C Sintered Pellets	74	80	0.15	0.16
1500°C Sintered Pellets	109	97	0.10	0.08

spectroscopic (XANES and EXAFS) techniques were employed to qualitatively analyze local structures and electronic charge symmetry. XANES is sensitive to the oxidation state and the coordination environment of absorbing atoms. Fig. 4 shows the room temperature recorded Hf-L₃ edge, Ho-L₃ edge, and Zr–K edge normalized spectra of XANES along with respective standards of HfO₂, Ho₂O₃, and ZrO₂. In XANES, the L₃-and K-edge resembles the transition of dipoles in $2P_{3/2}$ electrons to unoccupied $4d$ states, which correlates with the bond length, local environment, and coordination numbers of cations. The normalized XANES spectra of Ho, Hf, and Zr confirm the 3+, 4+, and 4+ oxidation states, respectively. But a minimal difference in the intensity counts of Ho (Fig. 4 (a)) and Zr (Fig. 4(b)) compared to their reference spectra indicates a complex local environment of the Hf–O and Zr–O polyhedral. However, substituting the Hf with Zr produced more stability in the Ho–O polyhedral [32,33]. This observation is inconsistent with the XRD analysis, as strong SSR was observed in the HZ samples. This complex polyhedral environment attributes to the transition of $1s$ electron to some unoccupied d state before the continuum, as the pre-edge (spectral feature) is observed immediately before the post-edge (absorption) in the case of transition metals. Furthermore, the pre-edge observed in the present case attributes to the 1s-t_{2g} and 1s-e_g octahedral field transitions, which are strongly related to metal ion site symmetry.

The local structure around the absorbing atom is obtained from qualitative analysis of EXAFS spectra. The χ(R) vs. R plots were generated using the Fourier transform of μ(E) versus E spectra following the methodology calculated from equations (2) and (3). Fig. 5 shows the Fourier transform spectra of HH and HZ samples. The theoretical EXAFS spectra were generated using the structural parameters of refined XRD patterns. The bond lengths (R), coordination numbers (N), and disorder factors (σ²) are refined and listed in Table 2.

The simultaneous fitting was carried out at both cation sites to reduce the number of independent parameters and improve the fitting statistics (see Table 2). Fig. 5(1) and 5(2) show that the intensity counts
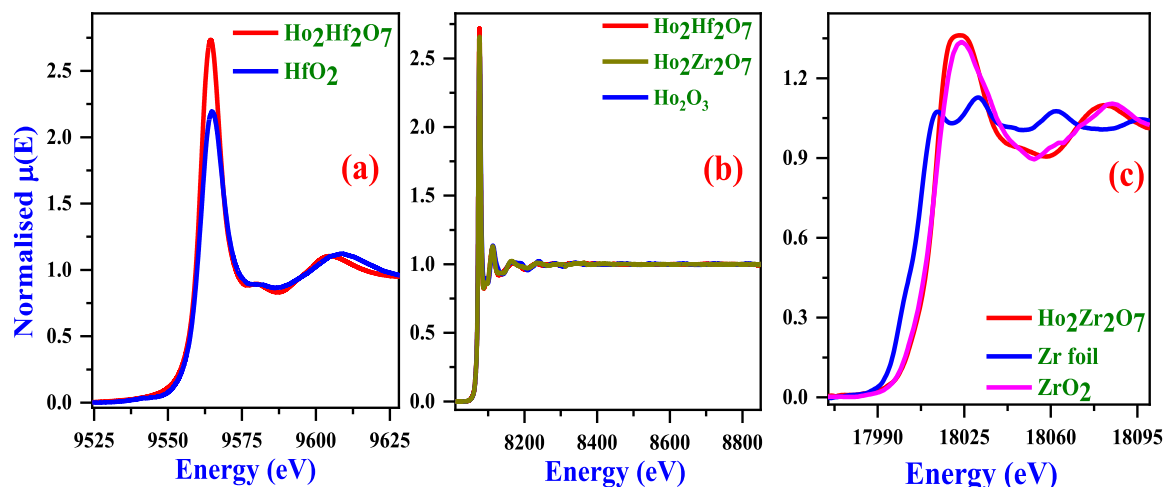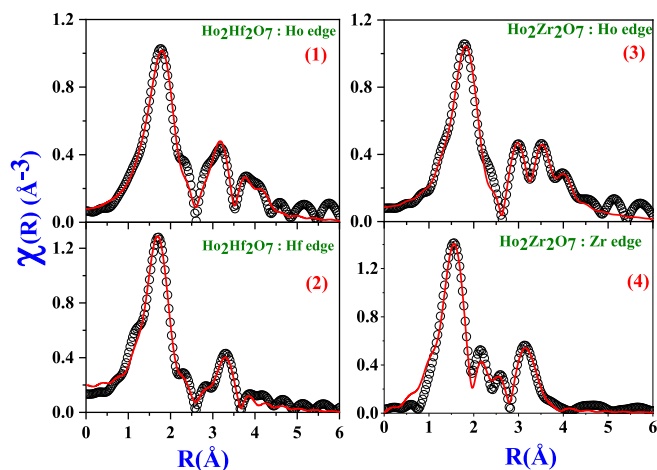

Fig. 5. Fourier transformed EXAFS spectra of (1) Ho-edge of HH, (2) Hf-edge of HH, (3) Ho-edge of HZ and (4) Zr-edge of HZ, respectively. Scattered points represent the experimental spectra, and the red colored curve represents the theoretical fit. (For interpretation of the references to color in this figure legend, the reader is referred to the Web version of this article.)

of the most intense peak at ~1.8 Å is constant, indicating a minimal influence on Ho–O polyhedral due to Zr-substitution. The multipath peaks of Ho–Ho, Ho–Hf, and Ho–Zr, are observed in the 2.5–5 Å, in which splitting in the HZ samples' plot indicates the gesture of lower disordering compared to HH. Fig. 5(3) and 5(4) show Hf-edge and Zr-edge fitting spectra, in which the mixing of the Zr–O peak with other multipath peaks evinces the complex coordination environment of the ZrO polyhedra. It was also observed in the XANES spectra (see Fig. 4 (c)), where HZ's Zr–K-edge spectra deviated from their reference counterpart.

Table 2 shows the relevant fitting results, in which a comparable Ho–O bond length is observed. It indicates that substituting B-site cations did not affect the AO-polyhedral; thus, we have a similar structure for both ceramics; Fd-3m. Also, this substitution leads to a comparable coordination state in HZ ceramics for Ho–O and Zr–O compared to the HH ceramics for Ho–O and Hf–O, resulting low disordering factor. The presence of Zr-atoms at the B-site reduces the overall disordering of the system. It was also evident in the XRD (Fig. 3) analysis, where more SSR was observed in HZ compared to the HH. Thus, it can be concluded that the substitution of Hf-ions by Zr-ions leads to ordering in the studied compounds. However, a complex coordination environment is observed for both HH and HZ ceramics. This complexity suggests a dominant

Fig. 4. Normalized XANES spectra (a) Hf- L₃ edge, (b) Ho- L₃ edge, and (c) Zr–K edge along with the standard oxide forms of HfO₂, Ho₂O₃, and ZrO₂.

Table 2
Bond length, coordination number, and disorder factor obtained by EXAFS fitting for $Ho_2Hf_2O_7$ and $Ho_2Zr_2O_7$.

$Ho_2Hf_2O_7$

Parameters	Path	Ho edge	Path	Hf edge
R (Å)	Ho–O	2.28 ± 0.01	Hf–O	2.14 ± 0.01
N		8.58 ± 0.98		5.61 ± 0.95
σ^2		0.0137 ± 0.0021		0.0088 ± 0.0015
R (Å)	Ho–Ho	3.57 ± 0.01	Hf–Hf	3.57 ± 0.01
N		6.44 ± 0.72		5.88 ± 0.74
σ^2		0.0143 ± 0.0017		0.0143 ± 0.0017
R (Å)	Ho–Hf	3.57 ± 0.01	Hf–Ho	3.57 ± 0.01
N		6.44 ± 0.72		5.88 ± 0.74
σ^2		0.0143 ± 0.0017		0.0143 ± 0.0017

$Ho_2Zr_2O_7$

Parameters	Path	Ho edge	Path	Zr edge
R (Å)	Ho–O	2.29 ± 0.02	Zr–O	2.10 ± 0.01
N		7.15 ± 1.07		7.76 ± 0.93
σ^2		0.0107 ± 0.0036		0.0040 ± 0.0015
R (Å)	Ho–Ho	3.55 ± 0.01	Zr–Zr	3.55 ± 0.01
N		5.37 ± 0.81		5.82 ± 0.69
σ^2		0.0075 ± 0.0019		0.0075 ± 0.0019
R (Å)	Ho–Zr	3.55 ± 0.01	Zr–Ho	3.55 ± 0.01
N		5.37 ± 0.81		5.82 ± 0.69
σ^2		0.0075 ± 0.0019		0.0075 ± 0.0019

nature of steric disordering over orbital disordering, which is common in cubic pyrochlores. This cationic/anionic disordering influences the charge transport behavior of the compounds.

3.3. Electrical analysis

3.3.1. Impedance behavior

Fig. 6(a–d) show the Nyquist plots of HH, and HZ compounds sintered at 1500 °C recorded over the temperature range 325–625 °C and in the frequency range 100 Hz -1 MHz. The semicircular arcs shown in the Cole-Cole plot provide essential details of the compounds' grain intrinsic and extrinsic contributions, grain boundaries, and electrode effects. The semicircular arcs centered below the abscissa indicate defect-driven resistivity in the studied compounds, valid at all temperatures. The evolution of two semicircles is observed for both compounds, suggesting the conductivity contribution of the grain and grain boundary, which is a strong function of temperature. To evaluate this, semi-circular arc were fitted with different circuits. (a) For temperature 325 °C and 425 °C, HH sample exhibits a single semi-circle in the measured frequency domain. The grain boundary value (R_{gb}) decreases with increasing temperature, which is an indication of considerable effect of space charge polarization of the ceramics. An increase in temperature improves the mobility of charge carriers and activates the thermally generated new charge carriers, further reducing the resistance value at higher temperatures. On the other-hand, HZ-325 °C, 425 °C, and 525 °C fit well using a series of two parallel RC circuits, showing the individual contribution of grain and grain boundary. R_g and R_{gb} values are decreasing with increasing temperature, which indicates a thermally activated process. Furthermore, the C_{gb} value increases with temperature, showing that the studied system retains its capacitive nature even at high temperatures.

(b) HH-525 °C showed two circles, indicating the individual effect of grain interior and grain boundary on the impedance behavior of the compound. HH-625 °C exhibited a huge circle whose center lies out of the real axis, indicating the resistive nature of the grain boundary and grain interior. The curve is fitted using a series combination of R_g with a parallel $R_{gb}C_{gb}$ circuit, as shown in Fig. 6 (c, d). The observed capacitance value is minimal, and the quality factor is near 1. HZ-625 °C fits well with a series combination of Rg and parallel $R_{gb}C_{gb}$-circuit. A very

minimal value of Rg and Rgb indicates the conductive feature of the compound at this temperature. The used fitting parameters are given in Table 3. Thus, it can be concluded that the HZ can retain its capacitive behavior in higher temperature regimes. The bulk contribution occurs at higher frequency whereas the grain boundary contribution is exhibited in the Cole-Cole plots at the lower frequency as seen in Fig. 6(a–d). The signal frequency decreases from left to right in the Cole-Cole plots shown in Fig. 6(a–d). Furthermore, the radius of the semicircles decreases as the temperature increases indicating the conduction mechanism in both the pyrochlore compounds is a thermally activated process. The results are consistent with previous reports [21–23].

3.3.2. Ionic conductivity

Temperature-dependent conductivity measurement was performed as a function of frequency to probe the nature of the ionic transport in HH and HZ ceramics similar to that described earlier by Kale et al. [34,35]. The temperature dependence of the ionic conductivity of HH and HZ ceramic can be expressed by the Arrhenius equation as follows:

$$\sigma = (\sigma_o) \exp(-E_a/kT) \tag{4}$$

$$\log(\sigma) = \log(\sigma_o) - (E_a/2.303*k) * (1/T) \tag{5}$$

Where σ is the conductivity in Scm^{-1}, k is the Boltzmann constant, T is the temperature in K and E_a is the activation energy in eV. Fig. 7 shows the Arrhenius plot of ionic conductivity ($\log \sigma$) as a function of the reciprocal of absolute temperature ($10^3/T$ (K)) of HH and HZ samples sintered at 1500 °C. Ionic conductivity shows a positive temperature coefficient, confirming that the mobility and hence the conductivity of oxide ions in the ceramic sample is a thermally activated process. In the solid electrolytes, the ionic conductivity is directly proportional to the extent of oxygen migration with the assistance of mobile oxygen vacancies [36]. In pyrochlore HH and HZ, sequential jumping of O_{48f}-O_{8a} site along HoO_6 polyhedral is the energetically most favorable pathway for the hopping of oxide ions. It is also well documented for pyrochlores with order/disorder transformation that cation occupy random sites and affects the site occupancy of anion leading to migration of oxygen from O_{48f}-O_{8b} position to fill O_{8ba} vacancy, which in turn leads to disordering with little impact on ionic conductivity. For higher disordering, delocalization of oxygen at O_{48f}-O_{8b} mediated by O_{8a} occurs at large scale depending upon synthesis process, and sintering conditions that promotes hopping and influences the conductivity of the compounds. In $Ho_2(Hf_{1-x}Zr_x)_2O_7$ sample, when Hf is replaced with Zr, it leads to more ordering in lattice, although the difference in ionic radii of tetravalent Hf^{4+} and Zr^{4+} is very small. The data of our EXAFS studies shown in Table 2 confirmed that the disordering factor of Zr–O in HZ was lower than Hf–O in HH sample, indicating that disordering was more stabilized in case of HZ than HH samples. Hence, it can be inferred that the structural stability and disordering present in the samples are determined by their bond-strength. An exponential increase in phonon frequency occurred when ionization energy increases, thereby increasing the structural rigidity and hence results in the formation of stronger bonds [37–39]. As the ionization energy of Zr is less than Hf, the Hf based systems exhibit greater bond strength and the observed activation energy of 1.37eV for HH and 0.98 eV for HZ, indicating a cation-anion mixed charge carrier hopping. Hence, it can be concluded that HH is more disordered than HZ, and therefore the observed activation energy for HH is greater than HZ [36–38]. Furthermore, we believe that Zr^{4+} occupies B-site in HZ, which improves anion sub-lattice ordering and ionic conductivity in present study of $Ho_2Zr_2O_7$ compared with $Ho_2Hf_2O_7$. Thus, the presence of Zr in the HZ system improves its cationic ordering, gives enhanced structural stability, and chiefly improves ionic conductivity. Furthermore, the data presented in Table 4 indicates that the pyrochlore compounds and their solid solution could be the potential ceramic materials for solid electrolyte application in the high temperature electrochemical devices such as solid oxide fuel cell, molten salt gas separation membranes and potentiometric or
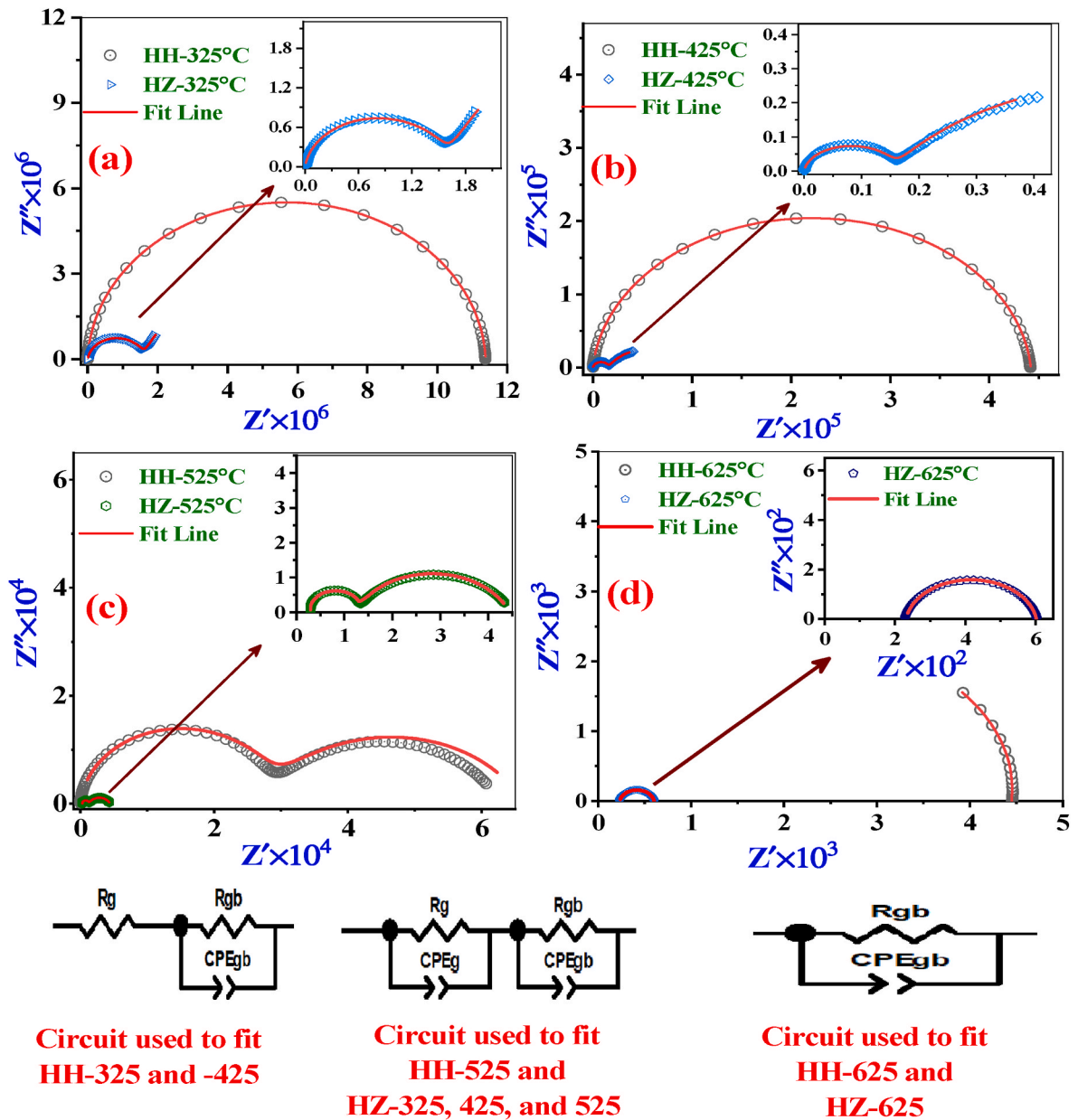
Fig. 6. Cole-Cole fit of impedance spectra of HH and HZ samples at (a) 325 °C, (b) 425 °C, (c) 525 °C, and (d) 625 °C. Black-colored curves show the HH plots, and red-colored curves show the HZ plots at various temperatures. The circuits used for fitting are shown in the diagram. (For interpretation of the references to color in this figure legend, the reader is referred to the Web version of this article.)

Table 3
Different parameters of Grain, and Grain boundary effects after fitting of EIS Spectra Sample.

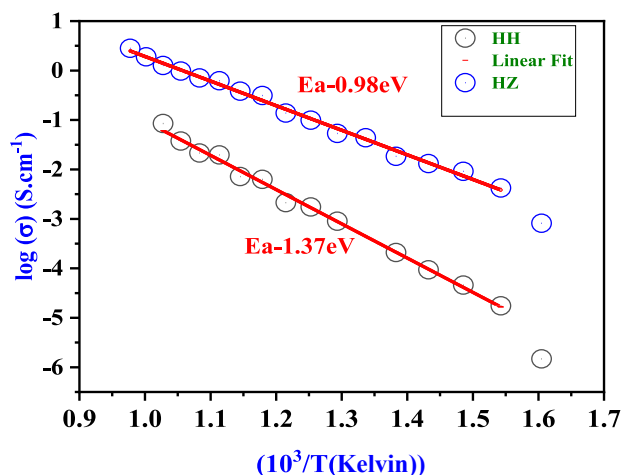| Sample Details	Grain Effect			Grain Boundary Effect		
	R_g (Ω)	C_g(F)	n_1	R_{gb}(Ω)	C_{gb}(F)	n_2
HH 325	1.38×10^6	1.41×10^{-11}	0.98	–	–	–
HZ 325	$1.5x \times 10^5$	7.2×10^{-11}	0.93	–	–	–
HH 425	4.42×10^5	1.8×10^{-11}	0.95	–	–	–
HZ 425	1.5×10^4	4.18×10^{-10}	0.94	–	–	–
HH 525	2.7×10^4	6.8×10^{-11}	0.96	3×10^4	5.34×10^{-8}	0.71
HZ 525	1.2×10^3	5.3×10^{-10}	0.95	4.7×10^3	1.7×10^{-6}	0.67

Fig. 7. Conductivity behavior of HH and HZ ceramics as a function of reciprocal of absolute temperature. The red colored lines show Arrhenius fit as per the given expression. (For interpretation of the references to color in this figure legend, the reader is referred to the Web version of this article.)

Table 4
Comparison of the ionic conductivity values of some known electrolyte materials at **500** °C.

Sr. No	Materials	Ionic Conductivity (S.cm^{-1})	Reference
01	Yttrium Stabilized Zirconia	7.2×10^{-4}	[40,41]
02	Gadolinium Doped Ceria	8.8×10^{-3}	[40,41]
03	$(Y_2O_3)_{0.08}(ZrO_2)_{0.92}$	1.1×10^{-3}	[42]
04	$Ce_{0.9}Gd_{0.1}O_{1.95}$	6.3×10^{-3}	[43]
05	Scandium Stabilized Zirconia	9.6×10^{-3}	[44]
06	$La_{0.9}Sr_{0.1}Ga_{0.9}Mg_{0.1}O_3$	6.3×10^{-3}	[45]
07	HH and HZ	9×10^{-4} and 5×10^{-2}	this work

amperometric gas sensors. Table 4 indicates that the conductivity of $Ho_2Zr_2O_7$ is comparable with the best-known fluorite oxide-ion conductor such as Sc_2O_3-stabilized ZrO_2 at 500 °C. The results of this study makes it even more interesting to investigate further the effect of substitution of Zr^{4+} for Hf^{4+} on crystal structure, spectroscopic properties and conductivity of the $Ho_2(Hf_{1-x}Zr_x)_2O_7$, $0 \leq x \leq 1$ solid solution series and similar other pyrochlore solid-solution systems.

4. Conclusion

In search of high stability pyrochlore materials as potential materials for solid electrolyte application, thermal stability of crystal structure over oxygen potential gradient and a reasonably high charge transport at elevated temperatures are few of the essential requirements. Based on this investigation, the compounds HH and HZ showed the potential candidature for this application. The aim was to study the effect of B-site cationic substitution on the background of the structural, local structure, and charge transport characteristics of HH and HZ. HZ is more suitable than HH, as it offers an ordered pyrochlore structure sintered at a lower temperature (1300 °C) than HH (1500 °C). A prominent SSR was observed in the XRD pattern of HZ compared to HH, which confirms the ordering of the pyrochlore phase. Although XANES and EXAFS spectra revealed a complex polyhedral environment for both ceramics, HZ is relatively less distorted than HH. The conductivity of $Ho_2Zr_2O_7$ obtained in this study is comparable with the best-known fluorite oxide-ion conductor such as Sc_2O_3-stabilized ZrO_2 at 500 °C as seen in Table 4. Temperature and frequency-dependent impedance spectroscopy and, the deduced conductivity behavior showed acceptable ionic

conductivity and lower activation energy of conduction of HZ ceramic compared with the HF. Thermally active charge carriers improve the charge transport characteristic of HZ at higher temperatures. These features make this system suitable for electrolyte applications in the intermediate temperature SOFCs.

Declaration of competing interest

The authors declare that they have no known competing financial interests or personal relationships that could have appeared to influence the work reported in this paper.

References

[1] A.P. Anantharaman, H.P. Dasari, Potential of pyrochlore structure materials in solid oxide fuel cell applications, Ceram. Int. 47 (2021) 4367, https://doi.org/10.1016/j.ceramint.2020.10.012.

[2] K. Eguchi, H. Kojo, T. Takeguchi, R. Kikuchi, K. Sasaki, Fuel flexibility in power generation by solid oxide fuel cells, Solid State Ionics 152–153 (2002) 411, https://doi.org/10.1016/S0167-2738(02)00351-X.

[3] Z. Zakaria, Z.A. Mat, S.H.A. Hassan, Y.B. Kar, A review of solid oxide fuel cell component fabrication methods toward lowering temperature, Int. J. Energy Res. 44 (2020) 594, https://doi.org/10.1002/er.4907.

[4] N. Mahato, A. Banerjee, A. Gupta, S. Omar, K. Balani, Progress in material selection for solid oxide fuel cell technology: a review, Prog. Mater. Sci. 72 (2015) 141, https://doi.org/10.1016/j.pmatsci.2015.01.001.

[5] T.A. Adams, J. Nease, D. Tucker, P.I. Barton, Energy conversion with solid oxide fuel cell systems: a review of concepts and outlooks for the short- and long-term, Ind. Eng. Chem. Res. 52 (2013) 3089, https://doi.org/10.1021/ie300996r.

[6] A.B. Stambouli, E. Traversa, Fuel cells, an alternative to standard sources of energy, Renew. Sustain. Energy Rev. 6 (2002) 295, https://doi.org/10.1016/S1364-0321(01)00015-6.

[7] Y. Zhu, W. Zhou, Y. Chen, Z. Shao, Enhancing electrocatalytic activity of perovskite oxides by tuning cation deficiency for oxygen reduction and evolution reactions, Angew. Chem. 128 (2016) 9134, https://doi.org/10.1021/acs.chemmater.5b04457.

[8] A. Chroneos, B. Yildiz, A. Taranc'on, D. Parfitt, J.A. Kilner, Oxygen diffusion in solid oxide fuel cell cathode and electrolyte materials: mechanistic insights from atomistic simulations, Energy Environ. Sci. 4 (2011) 2774, https://doi.org/10.1039/C0EE00717J.

[9] S.F. Wang, Y.W. Chen, Y.F. Hsu, Honeycomb oxygen-generator with doped bismuth-oxide-based electrolyte and Ag electrode, J. Electroceram. 44 (2020) 104, https://doi.org/10.1007/s10832-020-00202-x.

[10] S. Elangovan, J.J. Hartvigsen, L.J. Frost, Intermediate temperature reversible fuel cells, Int. J. Ceram. Technol. 4 (2007) 109, https://doi.org/10.1111/j.1744-7402.2007.02132.x.

[11] A.J. Feighery, J.T.S. Irvine, C. Zheng, High oxide ion conductivity in non-stoichiometric pyrochlores and fluorites in the ternary system ZrO₂ - Gd₂O₃ - TiO₂, Ionics 3 (1997) 30, https://doi.org/10.1007/BF02375521.

[12] A.N. Radhakrishnan, P.P. Rao, S.K. Mahesh, D.S. Vaisakhan Thamp, P. Koshy, Influence of disorder-to-order transition on lattice thermal expansion and oxide ion conductivity in (CaₓGd₁₋ₓ)₂(Zr₁₋ₓMₓ)₂O₇ pyrochlore solid solutions, Inorg. Chem. 51 (2012) 2409, https://doi.org/10.1039/C0DT01688H.

[13] S. Sumi, P. Prabhakar Rao, P. Koshy, Electrical transport properties of manganese containing pyrochlore type semiconducting oxides using impedance analyses, Mater. Res. Bull. 47 (2012) 4365, https://doi.org/10.1016/j.materresbull.2012.09.034.

[14] Y. Li, P.M. Kowalski, G. Beridze, A.R. Birnie, S. Finkeldei, D. Bosbach, Energetics of defects formation and oxygen migration in pyrochlore compounds from first principles calculations, Scripta Mater. 107 (2015) 18, https://doi.org/10.1016/j.scriptamat.2015.05.010.

[15] F.N. Sayed, D. Jain, B.P. Mandal, C.G.S. Pillai, A.K. Tyagi, Tunability of structure from ordered to disordered and its impact on ionic conductivity behavior in the Nd₂₋ᵧHoᵧZr₂O₇ (0.0 ≤ y ≤ 2.0) system, RSC Adv. 2 (2012) 8341, https://doi.org/10.1039/C2RA20458D.

[16] J. Shamblin, M. Feygenson, J. Neuefeind, C.L. Tracy, F. Zhang, S. Finkeldei, D. Bosbach, H. Zhou, R.C. Ewing, M. Lang, Probing disorder in isometric pyrochlore and related complex oxides, Nat. Mater. 15 (2016) 507, https://doi.org/10.1038/nmat4581.

[17] D.H. Prasad, J.W. Son, B.K. Kim, H.W. Lee, J.H. Lee, Synthesis of nano-crystalline Ce₀.₉Gd₀.₁O₁.₉₅ electrolyte by novel sol–gel thermolysis process for IT-SOFCs, J. Eur. Ceram. Soc. 28 (2008) 3107, https://doi.org/10.1016/j.jeurceramsoc.2008.05.021.

[18] Q.A. Islam, S. Nag, R.N. Basu, Study of electrical conductivity of Ca-substituted La₂Zr₂O₇, Mater. Res. Bull. 48 (2013) 3103, https://doi.org/10.1016/j.materresbull.2013.04.081.

[19] A.V. Shlyakhtina, N.V. Lyskov, A.N. Shchegolikhin, S.A. Chernyak, A.V. Knotko, I. V. Kolbanev, L.G. Shcherbakova, Structure evolution, ionic and proton conductivity of solid solutions based on Nd₂Hf₂O₇, Ceram. Int. 46 (2020) 17383, https://doi.org/10.1016/j.ceramint.2020.04.029.

[20] Z. Wang, G.M. Kale, M. Ghadiri, Novel ion-exchange process for the preparation of metal oxide nanopowders from sodium alginate, J. Am. Ceram. Soc. 95 (2012) 3124, https://doi.org/10.1111/j.1551-2916.2012.05366.x.

[21] S. Sardar, G.M. Kale, O. Cespedes, M. Ghadiri, Environmentally sustainable facile synthesis of nanocrystalline holmium hafnate (Ho$_2$Hf$_2$O$_7$): promising new oxide-ion conducting solid electrolyte, SN Appl. Sci. 2 (2020) 541, https://doi.org/10.1007/s42452-020-2336-9.

[22] S. Sardar, G.M. Kale, M. Ghadiri, O. Cespedes, Structural study of holmium zirconate nanoparticles obtained through carbon neutral sol-gel process, Thermochim. Acta 676 (2019) 120, https://doi.org/10.1016/j.tca.2019.04.003.

[23] S. Sardar, G.M. Kale, M. Ghadiri, Influence of processing conditions on the ionic conductivity of holmium zirconate (Ho$_2$Zr$_2$O$_7$), Ceram. Int. 46 (2020) 11508, https://doi.org/10.1016/j.ceramint.2020.01.177.

[24] Z. Wang, T.P. Comyn, M. Gadhiri, G.M. Kale, Maltose and pectin assisted sol–gel production of Ce$_{0.8}$Gd$_{0.2}$O$_{1.9}$ solid electrolyte nanopowders for solid oxide fuel cells, J. Mater. Chem. 21 (2011) 16494, https://doi.org/10.1039/C1JM12344K.

[25] S. Rahayu, J.S. Forrester, G.M. Kale, M. Gadhiri, Promising solid electrolyte material for an IT-SOFC: crystal structure of the cerium gadolinium holmium oxide Ce$_{0.8}$Gd$_{0.1}$Ho$_{0.1}$O1$_{.9}$ between 295 and 1023 K, Acta Crystallogr. C 74 (2018) 236, https://doi.org/10.1107/S2053229617017946.

[26] A.K. Poswal, A. Agrawal, A.K. Yadav, C. Nayak, S. Basu, S.R. Kane, C.K. Garg, D. Bhattacharyya, S.N. Jha, N.K. Sahoo, Commissioning and first results of scanning type EXAFS beamline (BL-09) at INDUS-2 synchrotron source, AIP Conf. Proc. 1591 (2014) 649, https://doi.org/10.1063/1.4872706.

[27] S. Basu, C. Nayak, A.K. Yadav, A. Agrawal, A.K. Poswal, D. Bhattacharyya, S.N. Jha, N.K. Sahoo, A comprehensive facility for EXAFS measurements at the INDUS-2 synchrotron source at RRCAT, Indore, India, J. Phys.: Conf. Ser. 493 (1–4) (2014) 012032, https://doi.org/10.1088/1742-6596/493/1/012032.

[28] F.A. Lopez-Cota, N.M. Cepeda-Sanchez, J.A. Diaz-Guillen, O.J. Dura, O.M.A. Lopez, M. Mczka, M. Ptak, A.F. Fuentes, Electrical and thermophysical properties of mechanochemically obtained lanthanide hafnates, J. Am. Ceram. Soc. 100 (2017) 1994, https://doi.org/10.1111/jace.14712.

[29] K.E. Sickafus, L. Minervini, R.W. Grimes, J.A. Valdez, M. Ishimaru, F. Li, K.J. Mcclellan, T. Hartmann, Radiation tolerance of complex oxides, Science 289 (2000) 748, https://doi.org/10.1126/science.289.5480.748.

[30] M. Pokhrel, S.K. Gupta, K. Wahid, Y. Mao, Pyrochlore rare-earth hafnate RE$_2$Hf$_2$O$_7$ (RE = La and Pr) nanoparticles stabilized by molten-salt synthesis at low temperature, Inorg. Chem. 58 (2019) 1241, https://doi.org/10.1021/acs.inorgchem.8b02728.

[31] L. Cong, S. Zhang, S. Gu, W. Li, Thermophysical properties of a novel high entropy hafnate ceramic, J. Mater. Sci. Technol. 85 (2021) 152, https://doi.org/10.1016/j.jmst.2021.02.005.

[32] K.M. Turner, D.R. Rittman, R.A. Heymach, C.L. Tracy, M.L. Turner, A.F. Fuentes, W.L. Mao, R.C. Ewing, Lanthanide stannate pyrochlores (Ln$_2$Sn$_2$O$_7$; Ln = Nd, Gd, Er) at high pressure, J. Phys. Condens. Matter 29 (2017) 504005, https://doi.org/10.1088/1361-648X/aa9960.

[33] S.P. Pavunny, Y. Sharma, K. Sudheran, S. Dugu, R.K. Katiyar, J.F. Scott, R.S. Katiyar, Holmium hafnate: an emerging electronic device material, Appl. Phys. Lett. 106 (1–5) (2015) 112902, https://doi.org/10.1063/1.4915503.

[34] G.M. Kale, T. Asokan, Electrical properties of cobalt-zinc ferrites, Appl. Phys. Lett. 62 (1993) 2324–2325, https://doi.org/10.1063/1.109405.

[35] Z. Wang, G.M. Kale, M. Ghadiri, Synthesis and characterization of Ce$_x$Gd$_{1-x}$O$_{2-\delta}$ nanopowders employing an alginate mediated ion-exchange process, Chem. Eng. J. 198 (2012) 149–153, https://doi.org/10.1016/j.cej.2012.05.063.

[36] C. Zhang, C.J. Li, G. Zhnag, X.J. Ning, C.X. Li, H. Liao, C. Coddet, Ionic conductivity and its temperature dependence of atmospheric plasma-sprayed yttria stabilized zirconia electrolyte, Mater. Sci. and Eng. B 137 (2007) 24–30, https://doi.org/10.1016/j.mseb.2006.10.005.

[37] A. Chandra, Temperature dependent ionic conductivity and cell performance studies of hot-pressed nanocomposite polymer electrolytes, Comput. Commun. 4 (2017) 33–39, https://doi.org/10.1016/j.coco.2017.04.001.

[38] G. Pilania, B. Puchala, B.P. Uberuage, Distortion-stabilized ordered structure in A2BB'O7 mixed pyrochlores, npj Comput. Mater. 5 (2019) 7, https://doi.org/10.1038/s41524-018-0144-1.

[39] F. Yang, Y. Wang, X. Zhao, P. Xiao, Enhanced ionic conductivity in pyrochlore and fluorite mixed phae yttrium doped lanthanum zirconate, J. Power Sources 273 (2015) 290, https://doi.org/10.1016/j.jpowsour.2014.09.067.

[40] D.J.L. Brett, A. Atkinson, N.P. Brandon, S.J. Skinner, Intermediate temperature solid oxide fuel cells, Chem. Soc. Rev. 37 (2008) 1568, https://doi.org/10.1039/B612060C.

[41] J. Zhang, C. Lesner, N.H. Menzler, O. Guillon, Comparison of solid oxide fuel cells (SOFC) electrolytes materials for operation at 500C, Solid State Ionics 344 (2020) 115138, https://doi.org/10.1016/j.ssi.2019.115138.

[42] T.- H Yeh, W.-C. Hsu, C.-C. Chou, J. Phys. IV 128 (2005) 213, https://doi.org/10.1051/jp4:2005128032.

[43] C. Xia, M. Liu, Microstructures, conductivities, and electrochemical properties of Ce0.9Gd0.1O2 and GDC–Ni anodes for low-temperature, SOFCs Solid State Ionics 152–153 (2002) 423, https://doi.org/10.1016/S0167-2738(02)00381-8.

[44] A. Kumar, A. Jaiswal, M. Sanbui, S. Omar, Oxygen-ion conduction in scandia-stabilized zirconia-ceria solid electrolyte (xSc$_2$O$_3$–1CeO$_2$–(99−x)ZrO$_2$, 5 ≤ x ≤ 11), J. Am. Ceram. Soc. 100 (2017) 659, https://doi.org/10.1111/jace.14595.

[45] T. Ishihara, H. Matsuda, Y. Takita, Doped LaGaO3 perovskite type oxide as a new oxide ionic conductor, J. Am. Chem. Soc. 116 (1994) 3801, https://doi.org/10.1021/ja00088a016.